Journal of Applied Polymer Science

# Interfacial crystallization of low-crystallinity elastomer incorporated by multi-walled carbon nanotubes: Mechanical reinforcement, structural evolution and enhanced thermal stability

**Siduo Wu, Guangsu Huang, Jinrong Wu, Hui Li**

College of Polymer Science and Engineering, State Key Laboratory of Polymer Materials Engineering, Sichuan University, Chengdu 610065, People's Republic of China

Correspondence to: G. Huang (E-mail: guangsu-huang@hotmail.com) and J. Wu (E-mail: wujinrong@scu.edu.cn)

**ABSTRACT:** In this paper, we report interfacial crystallization in olefin block copolymer (OBC) with low crystallinity incorporated by multi-walled carbon nanotubes (MWCNTs). A hybrid shish-kebab (HSK) superstructure in nanocomposites is observed that MWCNTs act as central shish and OBC crystals grow perpendicular to the nanotubes axis. The mechanical properties of nanocomposites are significantly improved with incorporation of MWCNTs. The most ideal reinforcing and toughening effect is both observed in nanocomposites with MWCNTs content of 1 wt % that can increase tensile strength by 122% as well as elongation at break by 36%. Efficient load transfer are confirmed with *in-situ* Raman spectra that *G'* band of MWCNTs in OBC matrix exhibit a downshifting trend and symmetric broadening of line shape which reveals additional macroscale strain from axial extension of MWCNTs in nanocomposites, thus suggesting a certain load is carried by HSK superstructure. The structural evolution of OBC and nanocomposites are investigated by *in-situ* wide-angle X-Ray Diffraction (WAXD). The Herman's orientation factor of nanocomposites with 2 wt % MWCNTs incorporation is lower than that of neat matrix at mall and intermediate strains, indicating a heterogeneous stress distribution and low compliance of HSK superstructure, which is consistent with *in-situ* Raman results. Moreover, the nanocomposites presents significantly enhanced thermal stability. The onset decomposition temperature of nanocomposites with 3 wt % MWCNTs can be 60.2°C higher than that of neat OBC. © 2015 Wiley Periodicals, Inc. J. Appl. Polym. Sci. **2015**, *132*, 42368.

**KEYWORDS:** composites; graphene and fullerenes; mechanical properties; nanotubes; structure-property relations; surfaces and interfaces

Received 15 February 2015; accepted 15 April 2015

**DOI: 10.1002/app.42368**

## INTRODUCTION

Due to extremely high aspect ratio, small dimension, superior mechanical and electrical properties, carbon nanotubes (CNT) is considered as an ideal filler for polymer composites.[1–9] In order to harness the excellent properties of CNTs in polymers, a strong interfacial adhesion between the matrices and CNTs is essentially crucial as well as a homogeneous dispersion of CNTs. To improve the interfacial interaction, strategies of macromolecular chain wrapping, covalent bonding and surface functionalization are generally adopted.[10–13] Nevertheless, these strategies need an additional step for the pretreatment of the CNTs surfaces, which is not cost-effective and scalable. An alternative strategy is interfacial crystallization that can be obtained *in-situ* during the processing process without any additional step, thus is convenient and scalable. For semicrystalline polymer composites, the fillers can act as nucleating agent and have the potential to induce or alter polymer crystallization, forming various hybrid crystalline structures such as transcrystallinity (TC), hybrid shish-calabash (HSC) and nanohybrid shish-kebab (NHSK).[11] For CNTs induced polymer crystallization, the geometric confinement brought by the curvature of small-diameter CNTs is often concluded as "soft epitaxy,"[14] by which enhanced interaction between polymer matrix and CNTs is achieved. Li *et al.* reported a NHSK superstructure via isothermal solution crystallization in polyethylene (PE)/CNTs and nylon 6,6/CNTs suspension, in which the polymer crystals periodically strung along the tube axis of CNTs that formed the shish, while polymer lamellae formed the kebabs.[15] The same hybrid crystalline structure with incorporation of CNTs via solution crystallization can also be achieved in polymers such as polyvinyl alcohol (PVA) and PE-b-PEO.[16,17] The most remarkable significance of hybrid crystalline structure obtained by interfacial crystallization is mechanical reinforcement, which is the most fundamental property of materials. For example, Fu Q. *et al.* reported the superior mechanical reinforcement in PE/multi-walled carbon nanotubes (MWCNTs) through formation of a shish-kebab

structure.[18–20] Nevertheless, studies of polyolefin elastomers (POEs) mainly focus on the blending systems of ethylene-octene copolymers,[21–24] few study on the interfacial crystallization of POEs has been done. A possible reason may be that traditional polyolefin elastomers, such as Ethylene-Octene Random Copolymers (ORC) and ethylene-propylene-diene monomer (EPDM), have statistical crystallizable block length and exhibit fringed micellar crystal morphology, which is not long enough to chain fold and form lamellar crystal structure.[25]

Synthesized by a chain shuttling technology, the INFUSE® olefin block copolymers (OBCs) exhibits highly ordered crystallizable hard blocks with low octene concentration and long soft blocks with high incorporation of octene.[26,27] As a promising substitute for traditional thermoplastic elastomers, OBCs exhibit many improved properties compared to random traditional POEs, e.g., higher crystallization rate, higher melting temperature and low melt viscosity. The reason for these improvements can be attributed to their unique block architecture and highly ordered lamellar crystalline structure,[28,29] which makes OBCs a potential matrix for interfacial crystallization with incorporation of nano-fillers.

Some study on the deformation and crystallization behavior of OBCs has been done. A sliplink model was used to describe the elasticity behavior of OBCs by Hiltner *et al.*, who considered that both sliplinks and crosslinks contributed to the stress–strain curve of OBCs. The sliplinks are mobile network junctions that restrict chain mobility until a sufficient force is applied, after which the crystal slippage starts to take place; while the crosslinks represent permanent junctions, possibly created by chain entanglements that tighten into rigid knots upon stretching.[25,28,29] The structure and morphology development of OBCs during deformation was studied by Hsiao *et al.* with *in-situ* synchrotron X-ray scattering and diffraction technique, and it was demonstrated that higher content of chain shuttling agents, shorter hard and soft blocks in each chain leaded to higher degree of orientation.[30,31] Wang *et al.* investigated the epitaxy crystallization of OBCs on the surfaces of polyolefins and benzoic acid, and found that the comonomer concentration difference between the hard and soft segments ($\Delta C_8$) as well as the crystallization conditions both strongly affected the epitaxy behaviors of OBCs on the substrates.[32,33] In our previous study, the inducing and nucleating effect of MWCNTs and graphene on the isothermal crystallization behavior of OBCs was also studied, we found that the equilibrium melting temperature of the nanocomposites was higher than that of the corresponding OBCs matrix, giving evidence that the crystals in the nanocomposites were more stable.[34] Yet, no research on the mechanical and thermal properties of OBCs based nanocomposites has been reported.

Due to relatively low crystallinity, the mechanical properties of OBCs (such as tensile strength and Young's modulus) are still not good enough to replace traditional styrene-based thermoplastic elastomers. Thus, achieving reinforcement via interfacial crystallization and incorporating OBCs with fillers of high aspect ratio and mechanical performance could be a potential way to solve this drawback. In this article, we prepare OBC/MWCNTs nanocomposites by a method of mixed-solvents blending. A HSK superstructure is observed which leads to efficient load transfer from OBC matrix to HSK superstructure. As a result, the mechanical properties and thermal stability of the OBC/MWCNTs nanocomposites are both significantly improved.

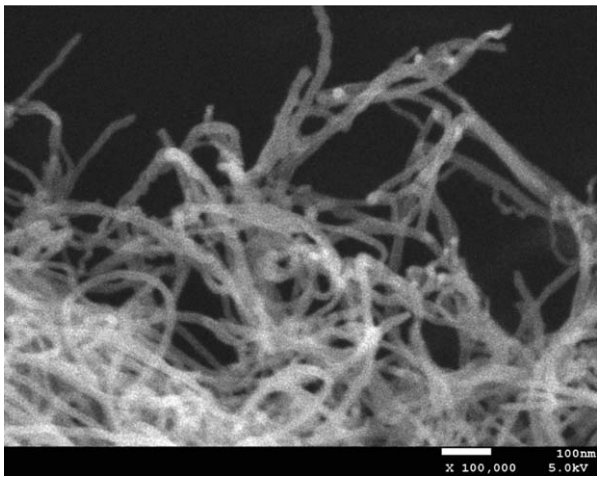


**Figure 1.** SEM image of raw MWCNTs.

## EXPERIMENTAL

### Materials

The OBC used in this study was from a local supplier with $M_w = 82600$ g/mol, $M_w/M_n = 2.3$, octene content = 12.9% and overall density of 0.878g/cm$^3$. MWCNTs of outer diameter ~20 nm, length 30–100 $\mu$m and specific area 180 $m^2 \cdot g^{-1}$ were purchased from Chengdu Organic Chemicals, R&D Center for Carbon Nanotubes of the Chinese Academy of Science. Scanning electron microscopy (SEM) image of raw MWCNTs are shown in Figure 1. Xylene (AR grade) and N,N-dimethyl formamide (DMF) (AR grade) were purchased from Chengdu Kelong Chemical Reagent Factory (China).

### Preparation of OBC/MWCNTs Nanocomposites

OBC pellets were dissolved in xylene at 130°C by magnetic stirring in an oil bath. MWCNTs were dispersed in DMF at a concentration of 1 mg/mL and sonicated for 2 h. The DMF/MWCNTs suspension was added dropwise into the xylene/OBC solution after sonication and the mixture was continuously stirred for another 10 min. The solvent was removed in a rotary evaporator and the mixture was further dried in a vacuum oven at 70°C for 48 h to remove the residual solvent. Nanocomposite samples were molded at 190°C into films of about 1 mm in thickness. The OBC/MWCNTs nanocomposites with 0.5 wt %, 1 wt %, 2 wt %, 3 wt % and 5 wt % MWCNTs were designated as CNT05, CNT1, CNT2, CNT3, and CNT5, respectively.

Before transmission electron microscope (TEM) measurements, the sample CNT2 was extracted by boiling xylene in a Soxhlet extractor for 48 h to remove the OBC matrix, the residual MWCNT suspension were dripped onto a copper grid. Before tensile and wide-angle X-ray diffraction (WAXD) test, samples of OBC and its nanocomposites were annealed in a vacuum oven at 110°C for 1 h to maturate crystallization in all samples.

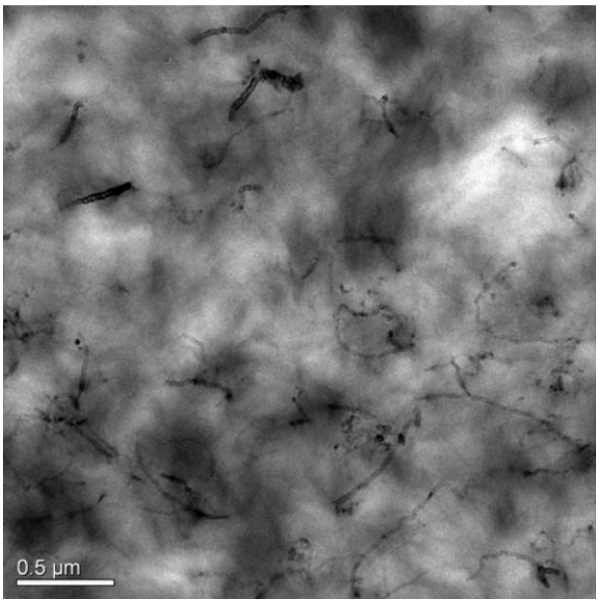


**Figure 2.** TEM image of OBC/CNT2.

### Characterization

Transmission electron microscopy (TEM) measurement (on FEI Tecnai G2 F20 S-TWIN) at an accelerating voltage of 200 kV was carried out to investigate the dispersion state of MWCNTs and morphology of Soxhlet extracted MWCNTs.

SEM measurement of raw MWCNTs and fractured surface of CNT2 were carried out on a X-650 Hitachi at an accelerating voltage of 20 kV.

DSC tests were performed on a Q200 (TA instruments) with nitrogen as the purge gas. The mass of the specimen was about 7–8 mg. The samples were heated to 190°C at 5°C/min, and holded for 5 min to eliminate any thermal history. Then the heat flow was recorded when the samples were cooled at 5°C/min to 40°C and then heated to 150°C at 5°C/min.

Tensile tests were carried out on an Instron 5567 universal testing machine with a 1000N-load cell at room temperature. All specimens of different concentrations of MWCNTs were tested with a gauge length of 20 mm and a displacement rate of 100 mm/min. Five samples were tested for each concentration.

*In-situ* Raman test were performed when specimen were extended to given strain. Raman spectra were recorded from 2300 to 3000 $cm^{-1}$ on a LABRAM HR800 confocal micro-Raman spectrometer using a 532 nm ND : YAG laser.

*In-situ* wide-angle X-ray diffraction studies were carried out at BL16B beamline at Shanghai Synchrotron Radiation Facility (SSRF). The wavelength used was 0.1237 nm. 2D WAXD patterns were collected by a MAR CCD X-ray detector (MAR-USA) with an acquisition time of 20 s for each data frame. The sample-to-detector distance was 159 mm. Uniaxial tensile deformation was performed with a home-made drawing machine. The samples were stretched symmetrically along the vertical direction with an initial gauge length of 20 mm and strain rate of 20 mm/min. Data analysis were done with the Fit2D software developed by European Synchrotron Radiation Facility (ESRF).

TGA tests were performed on a NETZSCH TG209 F3 to investigate the thermal stability of the OBC and nanocomposites. Specimens weighing approximately 10 mg were heated from 30 to 700°C at 5, 10, 15 and 20°C /min in flowing air. The weight loss was recorded as a function of temperature.

## RESULTS AND DISCUSSIONS

### Morphology and Dispersion of MWCNTs in Nanocomposites

TEM image of OBC/CNT2 in Figure 2 shows that MWCNTs are disentangled and finely dispersed in the matrix, suggesting that the mixed-solvents blending method is an effective way to prepare nanocomposites based on OBCs and MWCNTs. SEM images of the fractured surface of CNT2 are shown in Figure 3(a,b). The thick whiskers on the fractured surface could be MWCNTs wrapped by a thick polymer layer and are of an average diameter of over 60 nm, which is much larger than 20 nm of neat MWCNTs. The polymer layer on the surface of MWCNTs demonstrates strong interfacial interaction between MWCNTs and OBC matrix. The morphology of the Soxhlet extracted MWCNTs is shown in Figure 3(a,d), from which we can see a HSK superstructure formed by MWCNTs as central stems and OBC crystal lamellaes packing perpendicular to the nanotube axis. In our previous

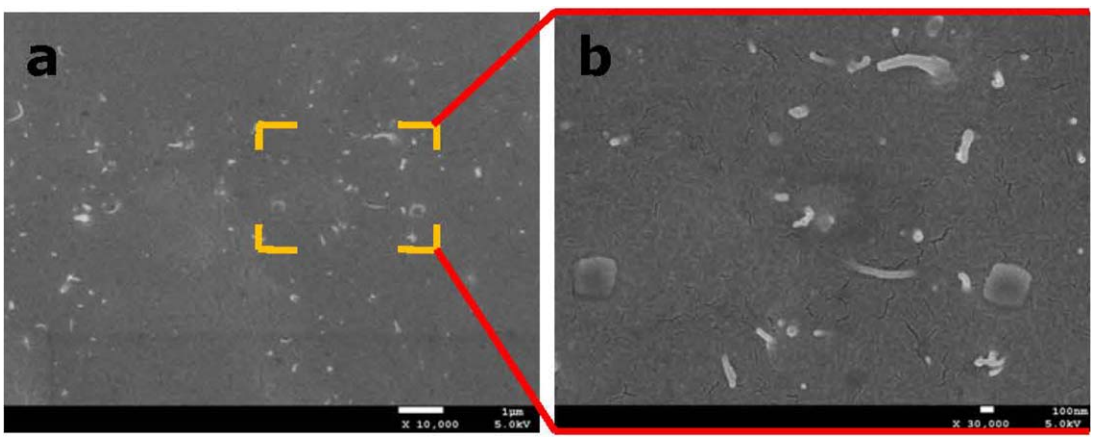


**Figure 3.** (a, b) SEM images of fractured surface of OBC/CNT2 (Figure 3b is the partial enlarged detail of Figure 3a). [Color figure can be viewed in the online issue, which is available at wileyonlinelibrary.com.]

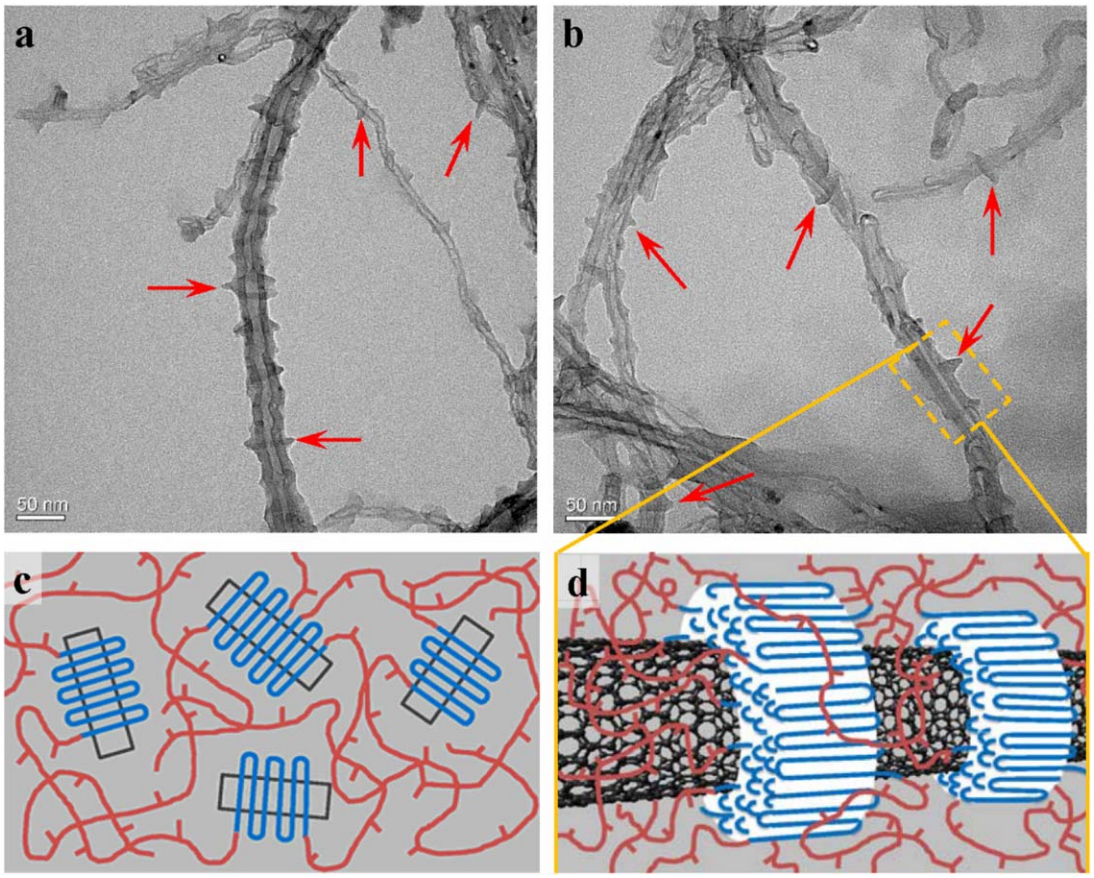


**Figure 4.** (a, b) TEM images of Soxhlet extracted MWCNTs (4a and 4b are of different views of extracted MWCNTs, the red arrows). Schematic diagrams of (c) crystallization of neat OBC and (d) crystallization of OBC in the presence of MWCNTs. [Color figure can be viewed in the online issue, which is available at wileyonlinelibrary.com.]

study, we have proposed that the hard segments of OBC prefer to align along the tube axis of one-dimensional MWCNTs, due to the size dependent soft epitaxy mechanism.[34] The schematic diagrams of crystallization of neat OBC and interfacial crystallization of OBC/MWCNTs nanocomposites are presented in Figure 4. Unlike HDPE or PA6 with large molecular weight and high crystallinities,[15,35] a HSK superstructure with a lateral dimension of kebab over 100 nm cannot be observed in the OBC/MWCNTs nanocomposites due to its low molecular weight of hard blocks ($M_{n,\text{hard}} \leq 4500$) and the covalent bonds between the hard and soft blocks. However, we can see in Figure 3(c,d) that the extracted MWCNTs still exhibit an kebab dimensionality of over 40 nm, obviously larger than 20 nm of neat MWCNTs. With direct evidence of HSK superstructure, we can conclude that if the crystallizable blocks in low-crystallinity polymers are long enough to chain fold and form crystal lamellae, observable interfacial crystallization can be achieved. The HSK superstructure contributes to strong interaction between OBC matrix and nanotubes, thus the total polymer–filler binding energy will be maximized for effective interfacial stress transfer,[36,37] which will be discussed in the mechanical reinforcement section.

### Crystallization Behaviors of OBC and Its Nanocomposites

The crystallization and subsequent melting curves of OBC and its nanocomposites are presented in Figure 5, from which the onset crystallization temperature $T_o$, crystallization peak temperature $T_{c,\text{peak}}$, melting temperature $T_m$ and crystallinity $X_c$ are obtained and listed in Table I, $X_c$ was obtained by comparing the heat of fusion of nanocomposites to that of 100% crystalline PE (292 J/g). An upward shift in the $T_c$ and $T_{c,\text{peak}}$ of OBC/

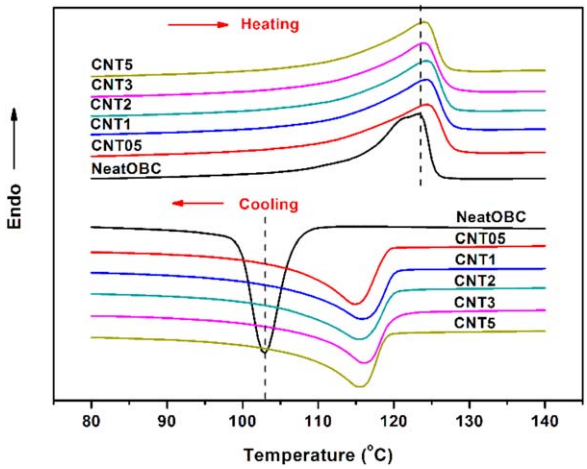


**Figure 5.** DSC thermograms of the crystallization and melting process of OBC and its composites. [Color figure can be viewed in the online issue, which is available at wileyonlinelibrary.com.]

**Table I.** Nonisothermal Crystallization and Melting Data of OBC and Its Nanocomposites

| Sample notation | $T_c$ (°) | $T_{c,peak}$ (°) | $T_m$ (°) | $X_c$ (%) |
|---|---|---|---|---|
| NeatOBC | 112.1 | 103.0 | 123.5 | 13.59 |
| OBC/CNT05 | 119.9 | 114.9 | 124.3 | 14.46 |
| OBC/CNT1 | 121.5 | 115.8 | 124.4 | 13.96 |
| OBC/CNT2 | 121.9 | 115.3 | 124.3 | 13.78 |
| OBC/CNT3 | 122.2 | 116.1 | 123.9 | 13.54 |
| OBC/CNT5 | 119.7 | 115.5 | 124.0 | 13.55 |

MWCNTs nanocomposites can be observed in Figure 5, indicating a strong heterogeneous nucleating effect of MWCNTs. The $T_c$ of OBC/CNT05 increases from 112.1°C to 119.9°C with incorporation of 0.5 wt % MWCNTs. However, further increase in the filler content doesn't give rise to notable increase in $T_c$, the possible reason for which might be that 0.5 wt % of MWCNTs is already sufficient for heterogeneous nucleation to facilitate the OBC crystallization. The $T_m$ of OBC/MWCNTs nanocomposites are also found to be enhanced, compared to that of neat OBC. As is well-known, low melt viscosity at high temperature is advantageous for chain packing and crystal growth, so a higher $T_{c,peak}$ always indicates the formation of thicker lamellae, and thus higher melting temperature.[38] Besides, the strong interfacial interaction resulting from the interfacial crystallization also makes crystals in the OBC/MWCNTs nanocomposites more thermally stable.[39]

As is reported in the filled semicrystalline polymer nanocomposites, additional nucleating surface generated by MWCNTs can lead to an increase in crystallinity. For example, the crystallinity of PVA with the addition of 0.6 vol % MWCNTs can be 17%, which is remarkably higher than 5% of neat PVA.[16] There is a little increase in crystallinity of the OBC/MWCNTs nanocomposites when the MWCNTs loading is below 3 wt %, due the nucleation effect of MWCNTs and the interfacial crystallization.[40–42] The increase in crystallinity is not very remarkable because the hard segment content in OBC chains is only 25%.

### Mechanical Reinforcement and Load Transfer

Stress–strain curves as well as histograms of tensile strength, Young's modulus and elongation at break for OBC and its nanocomposites are presented in Figure 6. Significant increase in the tensile strength is observed for the OBC/MWCNTs nanocomposites, for example, the tensile strength of CNT1 increase from 7.33 MPa to 16.33 MPa. This prominent increase can be attributed to the efficient interfacial stress transfer resulting from the interfacial crystallization. As is suggested by Hiltner *et al.*, sliplinks and cross-links both act as physical cross-link points that contribute to the mechanical strength of OBC. In the sliplink model, the stress response at low strains (i.e., under 200%) is governed primarily by the sliplink contribution, and a rapid decrease in the initial high modulus is observed with the onset of crystal lamellae slippage, which produces a yield-like plateau.[27] For the OBC/MWCNTs nanocomposites, the HSK superstructure is of lower compliance than dispersed lamellae in NeatOBC, thus higher load is needed for OBC nanocomposites to deform, leading to higher yield-like plateaus with incorporation of MWCNTs, as is presented in Figure 7. The higher yield-like plateau is also consistent with the remarkable increase in Young's modulus of the OBC/MWCNTs nanocomposites compared to that of neat OBC. For example, CNT3 has a Young's modulus up to 18.87 MPa, which is nearly threefold of 6.86 MPa of neat OBC. When the MWCNT loading is lower than 2 wt %, the elongation at break increases with increasing filler content, while it starts to decrease with further addition of MWCNTs. A probable reason might be that excessive MWCNTs can restrict the mobility of OBC chains. Nevertheless, even for the CNT5, the elongation at break is still slightly higher than that of neat OBC. Therefore, we can conclude that the HSK superstructure have both reinforcing and toughening effects on OBCs.

*In-situ* Raman measurements are further employed to unveil the load-bearing status of MWCNTs in nanocomposites. Figure 8(a) shows a typical *G'* band Raman spectra of OBC/CNT2 under strain, in which the downshifting trend of the peak position and the symmetric broadening of the line shape are the major characteristics of CNT2. From the downshift of *G'* Raman band, it can be inferred that compared to neat OBC, additional macroscale strain comes from axial extension of MWCNTs in nanocomposites, thus a certain load is carried by MWCNTs via interfacial adhesion.[43] The variation of the peak positions is summarized in Figure 8(b). When the strain is in the sliplink

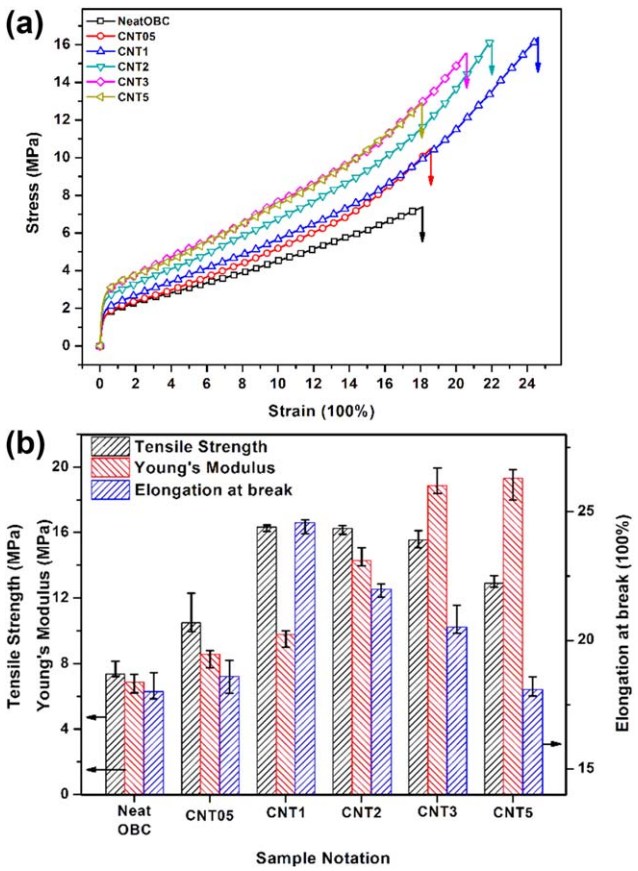


**Figure 6.** (a) Stress–strain curves and (b) Tensile strength, Young's modulus and elongation at break for OBC and its nanocomposites. [Color figure can be viewed in the online issue, which is available at wileyonlinelibrary.com.]

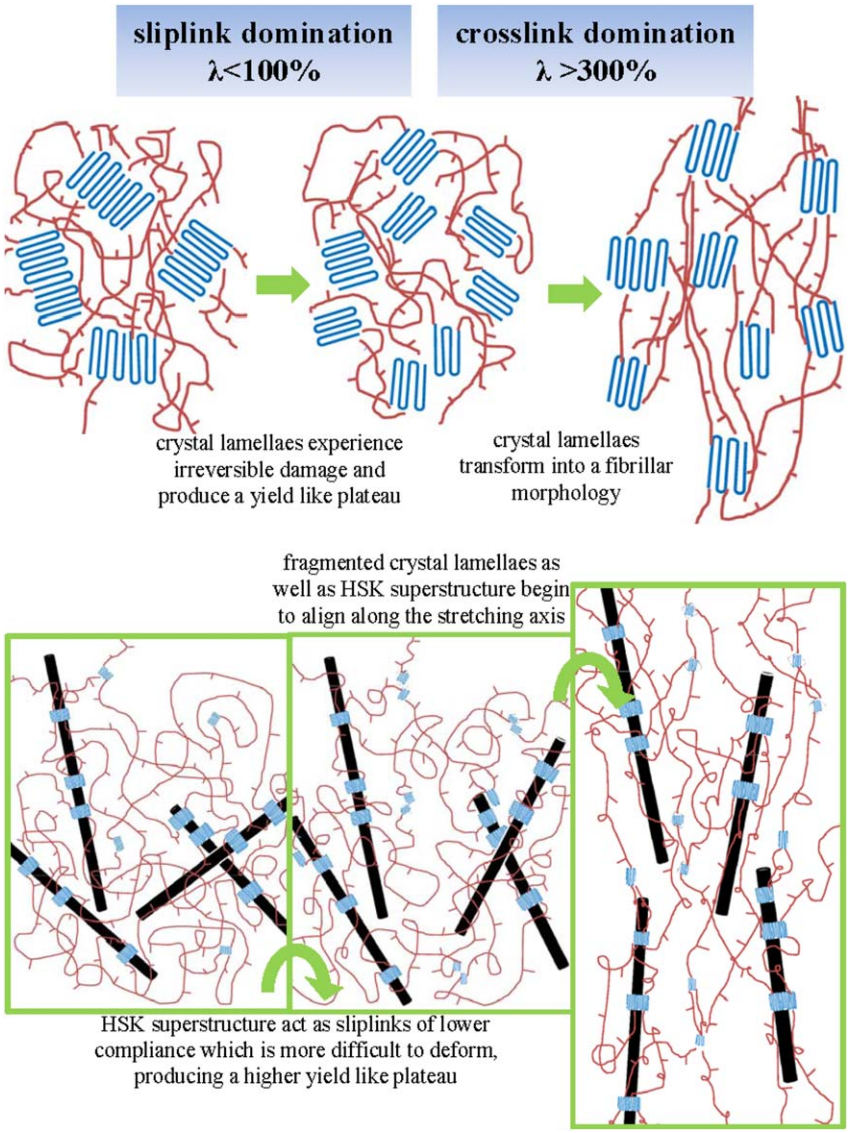


**Figure 7.** Schematic diagrams of the deformation process of OBC and nanocomposites. [Color figure can be viewed in the online issue, which is available at wileyonlinelibrary.com.]

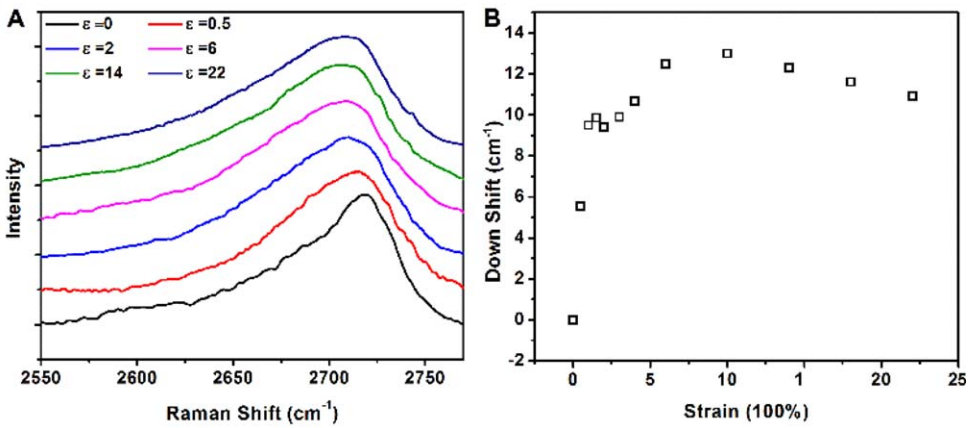


**Figure 8.** (A) Representative *G'* band Raman spectra of CNT2; (B) Downshifts of the peak position of *G'* band Raman spectra of CNT2. [Color figure can be viewed in the online issue, which is available at wileyonlinelibrary.com.]

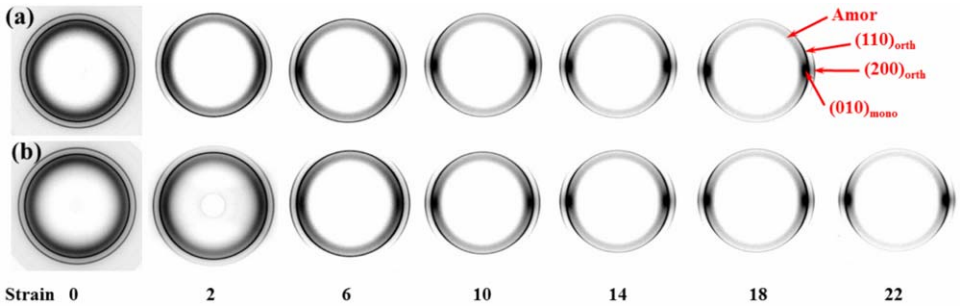


**Figure 9.** Selected 2D WAXD and SAXS patterns of (a) NeatOBC and (b) CNT2. [Color figure can be viewed in the online issue, which is available at wileyonlinelibrary.com.]

dominated region (<200%), the downshifts increase linearly with strain, which is consistent with a higher yield-like plateau in the stress–strain curves; when the strains are beyond 200%, downshifts of *G'* band plateau occurs until the final breakage, which is due to that after the nanotubes get sufficiently extended, the contribution of macroscale strain from the axial extension of MWCNTs reaches its maximum, thus the nanocomposites is more load-bearing.

### *In-Situ* WAXD Investigation

WAXD experiments were carried out to further investigate the structural changes of OBC and CNT2 during deformation process. In Figure 9, NeatOBC and CNT2 both exhibit isotropic rings of amorphous reflection as well as orthorhombic (110) and (200) reflections in unstretched state. While upon deformation, the isotropic rings of both orthorhombic crystal and amorphous phases gradually concentrate on the equator. The (010) reflection of the strain-induced monoclinic crystals emerges on the equator between amorphous ring and (110) reflection at the onset strain of 600%, exhibiting a highly ordered but relatively diffuse point-like reflection.[44]

Selected 1D WAXD profiles of NeatOBC and CNTB2 during deformation at different strains are shown in Figure 10. The total fraction of orthorhombic crystal phase of OBC and nanocomposites can be calculated by estimating the total area of (110) and (200) reflection.[44] The calculated fraction of orthorhombic crystals of NeatOBC and CNT2 is listed in Figure 11, from which we can see the orthorhombic fraction of both NeatOBC and CNT2 decrease with increasing strain. The fraction decrease is due to the fragmentation of crystal lamellae and transformation of orthorhombic crystal form into monoclinic crystals induced by uniaxial deformation. While during the whole deformation process, the fraction decrease of CNT2 is more gentle than that of NeatOBC. This could be due to the efficient load transfer brought by HSK superstructure that can

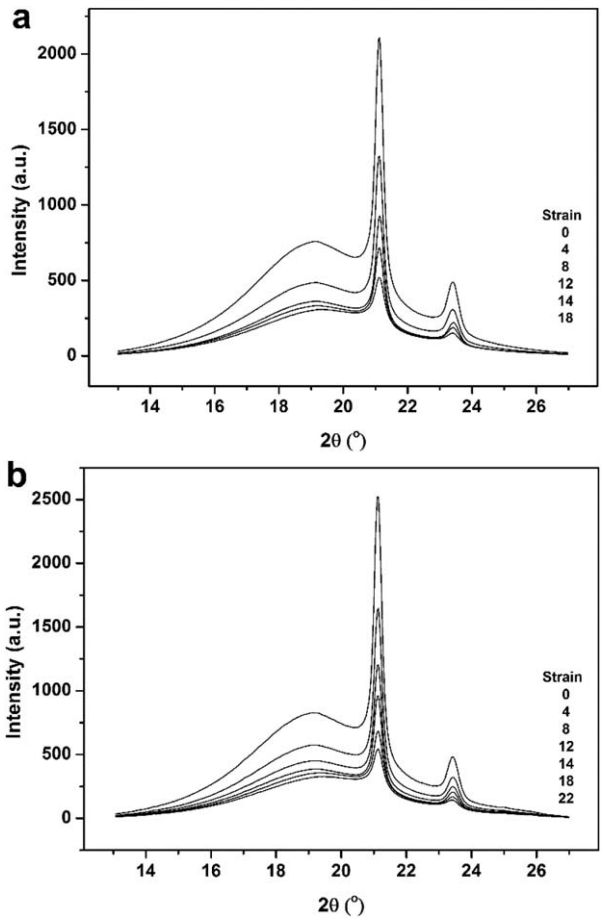


**Figure 10.** Selected 1D WAXD curves of (a) NeatOBC and (b) CNT2.

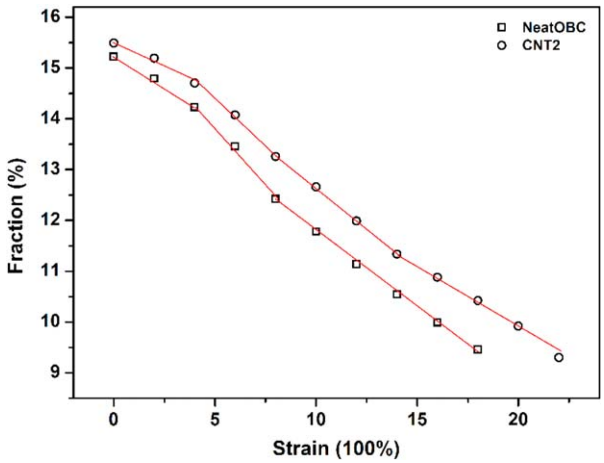


**Figure 11.** Fraction of orthorhombic crystal in NeatOBC and CNTB2 as a function of strain (the red solid lines are only a guide the eye). [Color figure can be viewed in the online issue, which is available at wileyonlinelibrary.com.]

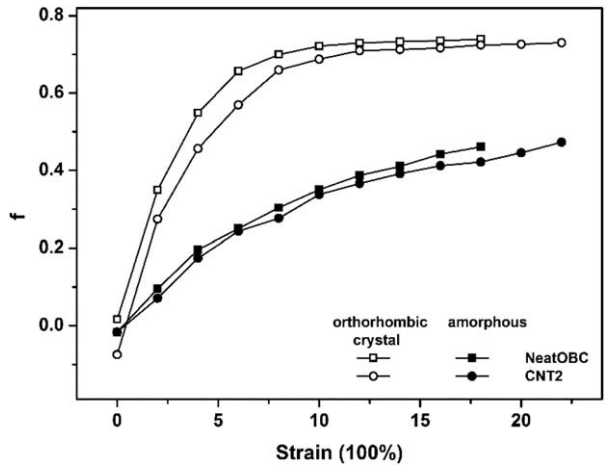


**Figure 12.** Hermans' orientation factors of orthorhombic crystal and amorphous phases of NeatOBC and CNT2 as a function of strain.

release the stress from the matrix, thus the fragmentation of lamellae in CNT2 is more gentle than that in NeatOBC. In addition, the kebabs on the nanotubes surface with higher dimensional stability could also contribute to the gentle decrease of orthorhombic crystal fraction of CNT2.

The orientation degree of orthorhombic crystal and amorphous crystal phases can be calculated by the Hermans' orientation function:[45]

$$f = \frac{3\ \cos^2\varphi - 1}{2}$$

where $\varphi$ is the angle between the chain axis and the stretching direction. $\langle \cos^2\ \varphi \rangle$ is defined as

$$\cos^2\varphi = \frac{\int_0^{\pi/2} I(\varphi)\ \cos^2\varphi \sin\varphi \mathrm{d}\varphi}{\int_0^{\pi/2} I(\varphi) \sin\varphi \mathrm{d}\varphi}$$

where $I(\varphi)$ is the scattered intensity along the angle $\varphi$. The value of $f$ is in the range of $-0.5$ to 1. $f = 1$ indicates perfect alignment of all polymer chains along stretching direction; $f = -0.5$ indicates perpendicular orientation to the stretching direction. The crystal orientation in this case can be indirectly obtained from the (110) and (200) reflections with the following expression[44]

$$\cos^2\varphi = 1 - 1.435\ \cos^2\varphi_{110} - 0.565\ \cos^2\varphi_{200}$$

The calculated $f$ value of amorphous phase was actually that of the normal vector of the amorphous chains, which need to be multiplied by $-2$ to convert the orientation factor ($-0.5$ to 0) into the value (1 to 0), which represents the degree of orientation along the deformation axis. The contribution from the (010) monoclinic reflection in the azimuthal intensity distribution can be perfectly subtracted by Gaussian peak fitting.

The calculated Hermans' orientation factors for orthorhombic and amorphous phases during deformation are presented in Figure 12. The $f$ values of orthorhombic crystals of both NeatOBC and CNT2 increase sharply at the strain range of 0–600%, after which the increase of $f$ values slows down till the crystal orientation of both samples reach their maximum at the strain of 1200%. The $f$ values of orthorhombic crystals of CNTB2 are relatively smaller than that of NeatOBC. As is reported, 1D fillers can bring heterogeneous stress distribution in polyolefin matrix, leading to reduced stress on crystals, thus the degree of orientation is lower; physical constraint effect of fillers can also reduce the degree of crystal orientation.[46,47] Our observation is consistent with previous reports. The HSK

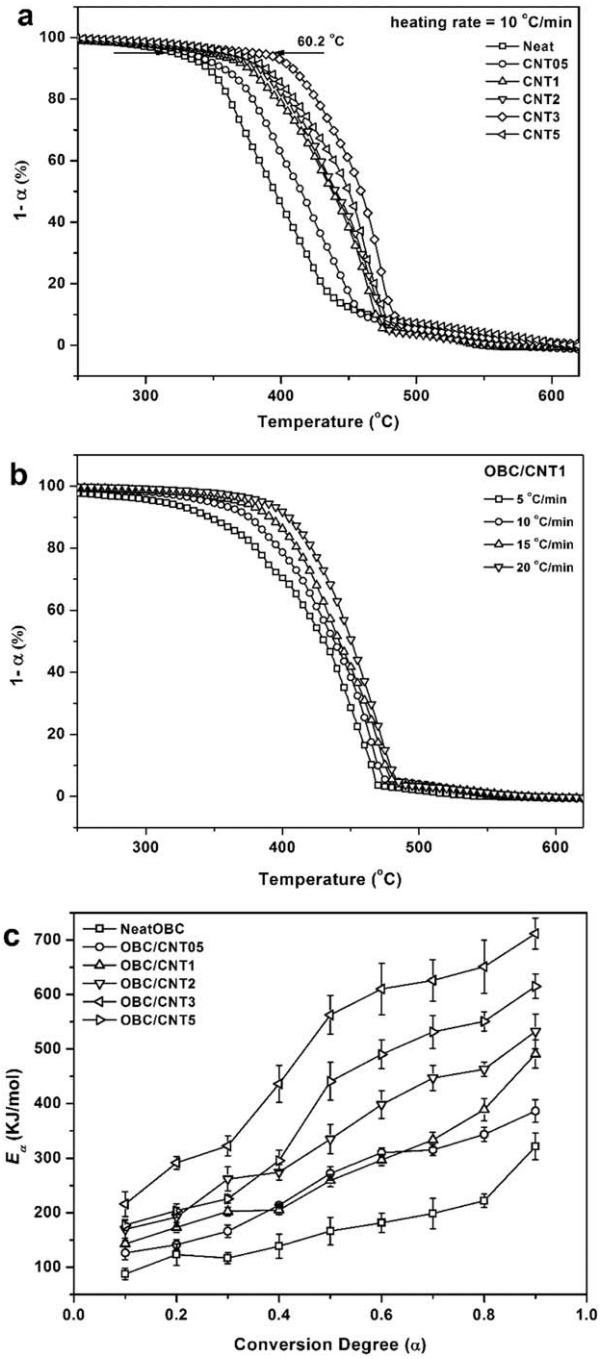


**Figure 13.** Representative TGA mass loss curves of (a) OBC and its nanocomposites at a heating rate 10°C /min (b) OBC/CNT1 at various heating rates in air flow and (c) dependence of activation energy ($E_\alpha$) on conversion degree ($\alpha$) of the mass loss as calculated with Friedman's method for OBC and its nanocomposites.

superstructure in CNT2 is of significantly larger dimensionality as well as lower compliance, thus the alignment of HSK superstructure into the stretching direction is more difficult than dispersed lamellae in NeatOBC, resulting in lower $f$ values. In CNT2, both HSK superstructure and dispersed lamellae in matrix can act as physical junctions, and the heterogeneous stress distribution has released a certain amount of stress from dispersed lamellae, thus the dispersed lamellae in CNT2 could also exhibit lower orientation. When the deformation strain exceeds 1200%, the orthorhombic crystal form in both NeatOBC and CNT2 is sufficiently oriented, in this region, the structure evolution is mainly about the extension of amorphous segments along the stretching direction. The fast orientation as low strains and slower orientation at higher strains is consistent with the *G'* band shifting in *in-situ* Raman spectra.

**Improvement in Thermal Stability**

TGA was used to characterize the thermal stability of OBC and its nanocomposites, as presented in Figure 13. The mass loss curves of OBC/MWCNTs nanocomposites notably shift toward higher temperatures compared to that of neat OBC. Taking the temperature of 5% weight loss as the onset decomposition temperature $T_d$, we can find that neat OBC starts to decompose at 321.6°C, while for OBC/CNT05, OBC/CNT1, OBC/CNT2, OBC/CNT3 and OBC/CNT5, the $T_d$ values increase to 331.8°C, 345.2°C, 355.7°C, 381.8°C, and 364.7°C, respectively. Thus, a maximum improve of 60.2°C in $T_d$ is obtained with 3 wt % MWCNTs. For OBC/CNT5, agglomeration caused by superabundant MWCNTs leads to a decrease of $T_d$ compared to that of OBC/CNT3. The decomposition activation energy ($E$) of OBC and its nanocomposites is determined by the Friedman method taking the logarithm of the conversion rate $d\alpha/dt$ as a function of the reciprocal temperature, in the form of:[48]

$$\ln\left(\frac{d\alpha}{dt}\right)_{\alpha,i} = \ln\left(\beta\frac{d\alpha}{dT}\right)_{\alpha,i} = \ln[f(\alpha)A_\alpha] - \frac{E_\alpha}{RT_{\alpha,i}}$$

where $\beta$ is the heating rate, $f(\alpha)$ is the conversion function and is considered as a constant, $R$ is the gas constant. By plotting $\ln(\beta d\alpha/dT)$ against $1/RT_{\alpha}$, the values of $E_\alpha$ are directly obtained and shown in Figure 13(c). OBC and its nanocomposites all show increased $E_\alpha$ as $\alpha$ increases, and the increasing magnitude is much higher for the OBC/MWCNTs nanocomposites at all mass conversions. The reason lies in the fact that CNTs are very efficient as free radical scavengers due to their high electron affinities.[49,50] Thus, as long as a uniform dispersion of MWCNTs in OBC is attained, the thermal stability of the nanocomposites can be remarkably enhanced.

## CONCLUSION

A HSK superstructure is achieved in OBC matrix with incorporation of MWCNTs that MWCNTs act as central shish and OBC crystals grow perpendicular to the nanotubes axis. MWCNTs have a strong nucleating effect on the OBC crystallization, which increases the crystallinity and melting temperature of the nanocomposites. The addition of MWCNTs significantly improves the mechanical property of the nanocomposites, and the optimal reinforcing and toughening effects are both observed in the nanocomposite with 1 wt % MWCNTs. Efficient load transfer is characterized by *in-situ* Raman spectra that *G'* band of MWCNTs in OBC matrix exhibit a downshifting trend and symmetric broadening of line shape which reveals additional macroscale strain from axial extension of MWCNTs in nanocomposites, thus suggesting a certain load is carried by MWCNTs via interfacial adhesion. With *in-situ* WAXD techniques, the structural changes of OBC and nanocomposites are investigated. The HSK superstructure with higher dimensional stability and larger dimensionality as well as the heterogeneous stress distribution brought by HSK superstructure leads to more gentle fraction decrease and slower orientation of orthorhombic crystal phase in OBC nanocomposites with incorporation of MWCNTs. Thermal stability is improved simultaneously in the presence of MWCNTs, and the improvement in decomposition temperature with 3 wt % filler loading can be 60.2°C higher than that of neat OBC, which might be due to strong free radical scavenging ability of MWCNTs.

## ACKNOWLEDGMENTS

The authors thank the National Basic Research Program (973 program) (No. 2011CB606000) for financial support.

## REFERENCES

1. Tasis, D. Carbon Nanotube-Polymer Composites. The Royal Society of Chemistry, **2013**; Chapter 4.
2. Bilalis, P.; Katsiqiannopoulos, D.; Avqeropoulos, A.; Sakellariou, G. *RSC Adv.* **2014**, *4*, 2911.
3. Panhuis, M. I. H. *J. Mater. Chem.* **2006**, *16*, 3598.
4. Geim, A. K.; Novoselov, K. S. *Nat. Mater.* **2007**, *6*, 183.
5. Novoselov, K. S.; Geim, A. K.; Morozov, S. V.; Jiang, D.; Zhang, Y.; Dubonos, S. V.; Grigorieva, I. V.; Firsov, A. A. *Science* **2004**, *306*, 666.
6. Novoselov, K. S.; Geim, A. K.; Morozov, S. V.; Jiang, D.; Katsnelson, M. I.; Grigorieva, I. V.; Dubonos, S. V.; Firsov, A. A. *Nature* **2005**, *438*, 197.
7. Sahoo, N. G.; Rana, S.; Cho, J. W.; Li, L.; Chan, S. H. *Prog. Polym. Sci.* **2010**, *35*, 837.
8. Panamoottil, S. M.; Potschke, P.; Lin, R. J. T.; Bhattacharyya, D.; Fakirov, S. *Exp. Polym. Lett.* **2013**, *7*, 607.
9. Hassani, A. J.; Mohd Ishak, Z. A.; Mohamed, A. R. *Exp. Polym. Lett.* **2014**, *8*, 177.
10. Yang, B. X.; Pramoda, K. P.; Xu, G. Q.; Goh, S. H. *Adv. Funct. Mater.* **2007**, *17*, 2062.
11. Baskaran, D.; Mays, J. W.; Bratcher, M. S. *Chem. Mater.* **2005**, *17*, 3389.
12. Moniruzzaman, M.; Chattopadhyay, J.; Billups, W. E.; Winey, K. I. *Nano Lett.* **2007**, *7*, 1178.
13. Ning, N. Y.; Fu, S. R.; Zhang, W.; Chen, F.; Wang, K.; Deng, H.; Zhang, Q.; Fu, Q. *Prog. Polym. Sci.* **2012**, *37*, 1425.
14. Ning, N. Y.; Luo, F.; Wang, K.; Zhang, Q.; Chen, F.; Du, R. N.; An, C. Y.; Pan, B. F.; Fu, Q. *J. Phys. Chem.* **2008**, *112*, 14140.
15. Li, C. Y.; Li, L. Y.; Cai, W.; Kodjie, S. L.; Tenneti, K. K. *Adv. Mater.* **2005**, *17*, 1198.

16. Zhang, F.; Zhang, H.; Zhang, Z. W.; Chen, Z. M.; Xu, Q. *Macromolecules* **2008**, *41*, 4519.
17. Yu, N.; Zheng, X. L.; Xu, Q.; He, L. H. *Macromolecules* **2011**, *44*, 3958.
18. Li, L. Y.; Li, C. Y.; Ni, C. Y. *J. Am. Chem. Soc.* **2006**, *128*, 1692.
19. Li, L. Y.; Li, C. Y.; Ni, C. Y.; Rong, L. X.; Hsiao, B. S. *Polymer* **2007**, *48*, 3452.
20. Li, L. Y.; Li, B.; Yang, G. L.; Li, C. Y. *Langmuir* **2007**, *23*, 8522.
21. Rana, D.; Kim, H. L.; Kwag, H.; Choe, S. *Polymer* **2000**, *41*, 7067.
22. Rana, D.; Kim, H. L.; Kwag, H.; Rhee, J.; Cho, K.; Woo, T.; Lee, B. H.; Choe, S. *J. Appl. Polym. Sci.* **2000**, *76*, 1950.
23. Rana, D.; Cho, K.; Woo, T.; Lee, B. H.; Choe, S. *J. Appl. Polym. Sci.* **1999**, *74*, 1169.
24. Rana, D.; Lee, C. H.; Cho, K.; Lee, B. H.; Choe, S. *J. Appl. Polym. Sci.* **1998**, *69*, 2441.
25. Bensason, S.; Hiltner, A.; Baer, E. *Macromolecules* **1997**, *30*, 2436.
26. Steve, P. C.; Kurt, W. S. *Prog. Polym. Sci.* **2008**, *33*, 797.
27. Arriola, D. J.; Carnahan, E. M.; Hustad, P. D.; Kuhlman, R. L.; Wenzel, T. T. *Science* **2006**, *312*, 714.
28. Wang, H. P.; Chum, S. P.; Hiltner, A.; Baer, E. *J. Appl. Polym. Sci.* **2009**, *113*, 3236.
29. Wang, H. P.; Hiltner, A.; Baer, E. *J. Polym. Sci.: Part B* **2009**, *47*, 1313.
30. Zuo, F.; Burger, C.; Chen, X. M.; Mao, Y. M.; Hsiao, B. S.; Chen, H. Y.; Marchand, G. R.; Lai, S. Y.; Chiu, D. *Macromolecules* **2010**, *43*, 1922.
31. Zuo, F.; Burger, C.; Chen, X. M.; Mao, Y. M.; Hsiao, B. S.; Chen, H. Y.; Marchand, G. R.; Lai, S. Y.; Chiu, D. *Macromolecules* **2011**, *44*, 3670.
32. Wen, T.; Zhou, Y.; Liu, G. M.; Wang, F. S.; Zhang, X. Q.; Wang, D. J.; Chen, H. Y.; Walton, K.; Marchand, G.; Loos, J. *Polymer* **2012**, *53*, 529.
33. Wen, T.; Liu, G. M.; Zhou, Y.; Zhang, X. Q.; Wang, F. S.; Chen, H. Y.; Loos, J.; Wang, D. J. *Macromolecules* **2012**, *45*, 5979.
34. Wu, S. D.; HLi, H.; Huang, G. S.; JWu, J. R. *RSC Adv.* **2014**, *4*, 19024.
35. Kodjie, S. L.; Li, L. Y.; Li, B.; Cai, W. W.; Li, C. Y. *J. Macromol. Sci. Part B* **2006**, *45*, 231.
36. Yang, J. H.; Wang, C. Y.; Wang, K.; Zhang, Q.; Chen, F.; Du, R. N.; Fu, Q. *Macromolecules* **2009**, *42*, 7016.
37. Kanagaraj, S.; Varanda, F. R.; Zhil'tsova, T. V.; Oliveira, M. S. A.; Simoes, J. A. O. *Compos. Sci. Technol.* **2007**, *67*, 3071.
38. Mai, F.; Wang, K.; Yao, M. J.; Chen, F.; Fu, Q. *J. Phys. Chem. B* **2010**, *114*, 10693.
39. Minus, M. L.; Chae, H. G.; Kumar, S. *ACS Appl. Mater. Interfaces* **2011**, *4*, 326.
40. Coleman, J. N.; Cadek, M.; Blake, R.; Nicolosi, V.; Ryan, K. P.; Belton, C.; Fonseca, A.; Nagy, J. B.; Gun'ko, Y. K.; Blau, W. J. *Adv. Funct. Mater.* **2004**, *14*, 791.
41. Ryan, K. P.; Lipson, S. M.; Drury, A.; Cadel, M.; Ruether, M.; O'Flaherty, S. M.; Barron, V.; McCarthy, B.; Byrne, J. B.; Blau, W. J.; Coleman, J. N. *Chem. Phys. Lett.* **2004**, *391*, 329.
42. Coleman, J. N.; Cadek, M.; Ryan, K. P.; Fonseca, A.; Nagy, J. B.; Blau, W. J.; Ferreira, M. S. *Polymer* **2006**, *47*, 8556.
43. Ma, W. J.; Liu, L. Q.; Zhang, Z.; Yang, R.; Liu, G.; Zhang, T. H.; An, X. F.; Yi, X. S.; Ren, Y.; Niu, Z. Q.; Li, J. Z.; Dong, H. B.; Zhou, W. Y.; Ajayan, P. M.; Xie, S. S. *Nano Lett.* **2009**, *9*, 2855.
44. Zuo, F.; Burger, C.; Chen, X. M.; Mao, Y. M.; Hsiao, B. S. *Macromolecules* **2010**, *43*, 1922.
45. Wilchinsky, W. Z. *J. Appl. Phys.* **1960**, *31*, 1969.
46. Chen, X. M.; Burger, C.; Fang, D. F.; Sics, I.; Wang, X. F.; He, W. D.; Somani, R. H.; Yoon, K.; Hsiao, B. S.; Chu, B. *Macromolecules* **2006**, *39*, 5427.
47. Chen, X. M.; Yoon, K.; Burger, C.; Sics, I.; Fang, D. F.; Hsiao, B. S.; Chu, B. *Macromolecules* **2005**, *38*, 3883.
48. Vyazovkin, S.; Burnham, A. K.; Criado, J. M.; Perez-Maqueda, L. A.; Popescu, C.; Sbirrazzuoli, N. *Thermochim. Acta* **2011**, *520*, 1.
49. Chrissafis, K. *Thermochim. Acta* **2010**, *511*, 163.
50. Watts, P. C. P.; Fearon, P. K.; Hsu, W. K.; Billingham, N. C.; Kroto, H. W.; Walton, D. R. M. *J. Mater. Chem.* **2003**, *13*, 491.